

Nano-patterning of Surfaces by Ion Sputtering: Numerical Study of the Anisotropic Damped Kuramoto-Sivashinsky Equation

E. Vitral^{a,*}, D. Walgraef^b, J. Pontes^a, G. R. Anjos^a, N. Mangiavacchi^a

^a*GESAR, Department of Mechanical Engineering, State University of Rio de Janeiro, Rio de Janeiro, RJ, 20940-903, Brazil*

^b*IFISC, University of Balearic Islands, Palma de Mallorca, Islas Baleares, 07122, Spain*

Abstract

Nonlinear models for pattern evolution by ion beam sputtering on a material surface present an ongoing opportunity for new numerical simulations. A numerical analysis of the evolution of preexisting patterns is proposed to investigate surface dynamics, based on a 2D anisotropic damped Kuramoto-Sivashinsky equation, with periodic boundary conditions. A finite-difference semi-implicit time splitting scheme is employed on the discretization of the governing equation. Simulations were conducted with realistic coefficients related to physical parameters (anisotropies, beam orientation, diffusion). The stability of the numerical scheme is analyzed with time step and grid spacing tests for the pattern evolution, and the Method of Manufactured Solutions has been used to verify the proposed scheme. Ripples and hexagonal patterns were obtained from a monomodal initial condition for certain values of the damping coefficient, while spatiotemporal chaos appeared for lower values. The anisotropy effects on pattern formation were studied, varying the angle of incidence of the ion beam with respect to the irradiated surface. Analytical discussions are based on linear and weakly nonlinear analysis.

Keywords: Ion beam sputtering, Damped Kuramoto-Sivashinsky, Method of Manufactured Solutions

1. Introduction

The present endeavor is interested in the spontaneous well-ordered periodicity developed by ion beam sputtering (IBS), which appears over a broad surface area under certain conditions [1]. Sputtering can be described as the ejection of atoms from a solid surface, as a result of energetic particle incidence. Among other

5 contemporary techniques in materials science, sputtering operates in nonequilibrium conditions, allowing the processing of nano-structures beyond the limitations imposed by equilibrium thermodynamics. Modeling the nonlinear evolution of sputter-eroded surfaces is an ongoing mechanical challenge. Our effort aims toward the development of a numerical scheme to solve an anisotropic Kuramoto-Sivashinsky equation with realistic coefficients, since it produces a rich zoology that can be adjusted to represent the aforementioned erosion

10 dynamics.

When the ion reaches the surface with a certain level of energy, a train of collision events may be established, resulting in the removal of atoms from that solid surface. The morphology of such surface can drastically change due to these sputtered atoms, and it might result in the formation of unexpectedly organized patterns, such as ripples, nanodots and hexagonal arrays of nanoholes (see Refs. [2, 3] for more 15 details). Valbusa et al. [4] discussed the interplay between ion erosion and vacancies on the surface reorganization, which would explain some of the patterns experimentally detected. The rate of energy deposition is a crucial parameter for the mechanisms, since high values can lead to a local transient melting of the surface [5], alongside the possibility of ion implantation.

*Corresponding author

Email address: eduardo.vitral@gmail.com (E. Vitral)

The Kuramoto-Sivashinsky equation appears from the continuum theories, in their attempt to describe
 20 surfaces eroded by ion bombardment, which would ultimately reproduce ripple formation and other organized
 patterns behavior. This equation was initially formulated to describe flame fronts and chemical waves
 [6], being capable of producing a great variety of morphologies for its highly nonlinear and deterministic
 character. Later it became a paradigm for pattern formation and spatiotemporal chaos, with a number of
 25 works devoted to it. Rost and Krug [7] describe the equation as being remarkable for the stabilization of the
 linear instability by the nonlinear term. This stabilization makes the equation a good candidate to represent
 the complexity behind the structure formation on sputtered surfaces, with a dynamic transiting between
 different regimes.

The isotropic damped Kuramoto-Sivashinsky (DKS) was previously studied by Paniconi and Elder [24].
 They numerically integrated the 2D equation through Euler's method (explicit) with a time step $\Delta t = 0.035$,
 30 since their aim was at a late-time long-aspect-ratio limit. For the spatial discretization with $\Delta x = 1.0$, a
 midpoint rule was adopted for the first order derivatives, and a stencil was used for the isotropic discrete
 Laplacian. Results obtained when changing the damping coefficient were analyzed, but the model was not
 physically linked to any particular phenomenon. Fcsko et al. [14] became interested in the 2D isotropic
 35 DKS due to its stationary solutions showing a remarkable resemblance to IBS patterns. They connected
 these solutions to the hexagonal patterns found on a GaSb(100) surface after ion erosion. In terms of
 numerics, they also used Euler's method for time integration and spatially discretized the Laplace operator
 through eight nearest neighbors, and the spatial and time steps where $\Delta x = 1.0$ and $\Delta t = 0.01$.

Here we perform a numerical study of patterning by IBS through a model that corresponds to a DKS
 40 equation for an anisotropic system with realistic coefficients. Our proposed model is close to a previous
 expansion of the Bradley and Harper theory performed by Makeev et al. [6], and also to the form found in
 Fcsko and Keller [13], but contains terms to account for various anisotropies and adopts some simplifications
 (as isotropic energy distribution for the atomic cascade). Since the equation is very sensitive to its parameters
 45 value, there is still much to be explored when it comes to its behavior in 2D, especially when working in
 the range of physical experimental data. Our goal is to understand the evolution of a material surface
 displaying a preexisting pattern under IBS through this model. We look into the growth and competition
 between modes for different initial patterns, which are compared with analytical results from a developed
 linear and weakly nonlinear analysis. Also, we study the connection between the beam angle and the
 50 relative anisotropy found on the patterns, and provide an insight on the role of the damping term under our
 particular model and coefficients. This way, we introduce tools and a new way to interpret experimental
 results, from ripples to coarsening in the nonlinear regime.

Stability requirements impose restrictive limitations to the time step on explicit schemes, especially in
 the presence of fourth-order derivatives. At the same time, implementation of straight implicit schemes
 for 2 or more dimensions leads to a large system of linear equations, which might not be a suitable cost-
 efficient option. Therefore, in Sec. 2 we propose a finite-difference semi-implicit splitting scheme of second
 55 order in time and space to numerically solve this anisotropic DKS equation subjected to periodic boundary
 conditions. The computational domain is a two dimensional surface characterized by a height function
 $h(x, y, t)$, whose evolution in time is monitored. Internal iterations are used inside each time step to enhance
 the approximation of the nonlinear term.

Previously, a similar numerical scheme has been successfully implemented for Swift-Hohenberg [8, 9],
 60 which is a fourth-order parabolic equation, dealing with the same challenges of high-order spatial derivatives
 and nonlinearity. The coordinate splitting, alongside the half-time steps (with only one of the operators
 implemented explicitly), were proven to be an effective approach for such equation, combining desirable
 stability properties with efficient computational costs. We show that this is also true for our case, such that
 the scheme remains stable for time steps much larger than the reported ones for explicit methods.

Section 3 deals with a linear analysis to study the system's response to small perturbations, followed by
 a weakly nonlinear analysis in Sec. 4. The numerical scheme is verified by the Method of Manufactured
 Solutions (MMS) in Sec. 5, and its stability is analyzed in Sec. 6 with time step and grid spacing tests for
 the pattern evolution. Preexisting structures are employed as initial conditions, varying from a monomodal
 to a random initial pattern.

We then further discuss how the realistic coefficients fit in the model in Section 7, where simulation

results are shown for a high temperature case. In such system, sputtering terms and diffusion act on similar scale, and should agree with our qualitative analysis for pattern selection. There, we study the circumstances under which hexagonal patterns emerge, and how the damping coefficient α relates to the organizational degree of the structure (even for spatiotemporal chaos). Finally, we analyze the effects of variations of the angle of incidence of the beam θ , and also a scenario where the nonlinear terms compensate each other.

75

2. Mathematical Modelling and Numerical Scheme

2.1. Governing Equation

In order to solve the anisotropic DKS equation which emerges from the IBS modelling [4, 6, 10, 11, 12], a second order in time finite difference numerical scheme is proposed. The general model takes into account realistic coefficients corresponding to anisotropies, diffusion, beam orientation and others. For the case of isotropic energy distribution, considering an ion beam with angle of incidence θ with respect to the normal of the surface ($\theta = 0$ for normal incidence), the evolution of the surface height h is governed by:

$$\begin{aligned} \frac{\partial h}{\partial t} = & -\alpha_o h + \frac{Fa}{2} \left(\mu \frac{\partial^2 h}{\partial x^2} + \nu \frac{\partial^2 h}{\partial x^2} \right) + \frac{Fa_\eta^2}{2} \left(\nu_x \left(\frac{\partial h}{\partial x} \right)^2 + \nu_y \left(\frac{\partial h}{\partial y} \right)^2 \right) \\ & + \frac{Fa^3}{8a_\eta^2} \left(D_{XX} \frac{\partial^4 h}{\partial x^4} + D_{XY} \frac{\partial^4 h}{\partial x^2 \partial y^2} + D_{YY} \frac{\partial^4 h}{\partial y^4} \right) \\ & - K \left(\frac{\partial^4 h}{\partial x^4} + 2 \frac{\partial^4 h}{\partial x^2 \partial y^2} + \frac{\partial^4 h}{\partial y^4} \right) \end{aligned} \quad (1)$$

Here, $F = \frac{J\epsilon p}{\sqrt{2\pi}\eta} \exp\left(\frac{-a_\eta^2 c^2}{2}\right)$, where J is the flux of bombarding ions, ϵ is the energy carried by the ions, p is associated to the surface binding energy and scattering cross-section, a is the penetration depth, and η is the width of energy distribution. The parameter K takes into account the surface diffusion effects, which vary with temperature. In terms of realistic values, ϵ lies between 0.1 and 100 keV, while some examples for the others are: $J \approx 10^{15} \text{ cm}^{-2} \text{s}^{-1}$, $p \approx 2$, $a \approx 2 \text{ nm}$, $\eta \approx 0.5 \text{ nm}$, and $K \approx 34 \times 10^{-28} \text{ cm}^4 \text{s}^{-1}$ [6, 13]. Additionally, c and s represent the cosine and sine of θ , and a_η is the ratio a/η . In standard form, the equation reads:

$$\begin{aligned} \frac{\partial \bar{h}}{\partial \tau} = & -\alpha \bar{h} + \mu \frac{\partial^2 \bar{h}}{\partial X^2} + \nu \frac{\partial^2 \bar{h}}{\partial Y^2} + \bar{\nu}_x \left(\frac{\partial \bar{h}}{\partial X} \right)^2 + \bar{\nu}_y \left(\frac{\partial \bar{h}}{\partial Y} \right)^2 + D_{XX} \frac{\partial^4 \bar{h}}{\partial X^4} \\ & + D_{XY} \frac{\partial^4 \bar{h}}{\partial X^2 \partial Y^2} + D_{YY} \frac{\partial^4 \bar{h}}{\partial Y^4} - \bar{K} \left(\frac{\partial^4 \bar{h}}{\partial X^4} + 2 \frac{\partial^4 \bar{h}}{\partial X^2 \partial Y^2} + \frac{\partial^4 \bar{h}}{\partial Y^4} \right) \end{aligned} \quad (2)$$

90 where \bar{h} and τ are, respectively, the dimensionless surface height function of the external atom layer and the time dependency of the transient model, with X and Y as the domain space coordinates. They relate to their dimensional counterpart via: $\bar{h} = \frac{a^2}{a_\eta^2} h$, $X = \frac{2a_\eta}{a} x$ (similarly for Y), $\tau = \frac{2Fa_\eta^2}{a} t$, $\alpha = \frac{a}{2Fa_\eta^2} \alpha_o$, and $\bar{K} = \frac{8a_\eta^2}{Fa^3} K$. Equation 2 presents a damping term $-\alpha \bar{h}$, with α being a positive damping coefficient, which was initially proposed as a contribution of the redeposition mechanism to the formation of nanodots [14]. However, Bradley [15] demonstrated that the redeposition of sputtered material is a nonlinear effect observed in pattern formation by IBS, discarding the influence of this physical mechanism on the appearance of hexagonal ordered structures. Nevertheless, we maintain our interest in the linear damping term for the

sake of producing stable patterns and supressing the emergence of chaos . Finally, the parameters μ , $\bar{\nu}_x$, $\bar{\nu}_y$, D_{XX} and D_{XY} will be defined as follows (see Makeev et al. [6] for further details):

$$\begin{aligned}\mu &= 2s^2 - c^2 - a_\eta^2 s^2 c^2 & \nu &= -c^2 \\ \bar{\nu}_x &= c \left(3s^2 - c^2 - a_\eta^2 s^2 c^2 \right) & \bar{\nu}_y &= -c^3 \\ D_{XX} &= -\left(c^2 - 4s^2 + 2a_\eta^2 s^2 \left(c^2 - \frac{2}{3}s^2 \right) + \frac{a_\eta^4}{3}s^4 c^2 \right) & D_{YY} &= c^2 \\ D_{XY} &= 2 \left(c^2 - 2s^2 + a_\eta^2 s^2 c^2 \right) .\end{aligned}$$

These parameters are responsible for introducing various types of anisotropies. Now, in order to solve Eq. 2, the following second order in time Crank-Nicolson semi-implicit scheme was adopted:

$$\frac{\bar{h}^{n+1} - \bar{h}^n}{\Delta\tau} = \Lambda_X \left(\frac{\bar{h}^{n+1} + \bar{h}^n}{2} \right) + \Lambda_Y \left(\frac{\bar{h}^{n+1} + \bar{h}^n}{2} \right) + f^{n+1/2}. \quad (3)$$

The superscript $(n+1)$ refers to the current time and (n) to the previous one. The operators Λ_X , Λ_Y (both modified from Eq. 3 to account for the division by two) and the function $f^{n+1/2}$ are defined as:

$$\begin{aligned}\Lambda_X &= \frac{1}{2} \left[-\frac{\alpha}{2} - (D_{XX} + K) \frac{\partial^4}{\partial X^4} \right] \\ \Lambda_Y &= \frac{1}{2} \left[-\frac{\alpha}{2} - K \frac{\partial^4}{\partial Y^4} \right] \\ f^{n+1/2} &= \frac{1}{2} \left[\bar{\nu}_x \left(\frac{\partial \bar{h}^{n+1}}{\partial X} + \frac{\partial \bar{h}^n}{\partial X} \right) \frac{\partial}{\partial X} + \bar{\nu}_y \left(\frac{\partial \bar{h}^{n+1}}{\partial Y} + \frac{\partial \bar{h}^n}{\partial Y} \right) \frac{\partial}{\partial Y} + \mu \frac{\partial^2}{\partial X^2} \right. \\ &\quad \left. + \nu \frac{\partial^2}{\partial Y^2} + (D_{XY} - 2K) \frac{\partial^4}{\partial X^2 \partial Y^2} + D_{YY} \frac{\partial^4}{\partial Y^4} \right] (\bar{h}^{n+1} + \bar{h}^n) .\end{aligned}$$

2.2. Internal Iterations

Internal iterations at each time step are required to secure the approximation for the nonlinearities taking part in the scheme of Eq. 3. The iterations loop will continue until the L_∞ norm points that the convergence was attained. There is a trade-off related to the time step $\Delta\tau$: for a larger $\Delta\tau$, convergence will be impaired and the number of internal iterations will increase, while a smaller $\Delta\tau$ will impact on a smaller number of iterations, but it will imply on a greater number of time steps. The internal iterations scheme reads:

$$\frac{\bar{h}^{n,m+1} - \bar{h}^n}{\Delta\tau} = \Lambda_X (\bar{h}^{n,m+1} + \bar{h}^n) + \Lambda_Y (\bar{h}^{n,m+1} + \bar{h}^n) + f^{n+1/2} \quad (4)$$

where the index (m) refers to the internal iteration number. The superscript $(n, m+1)$ identifies the new iteration, while (n) are the values of the previous time step. The superscript $(n+1)$ for the nonlinear term

in the function $f^{n+1/2}$ will be replaced by (n, m) , which stands for the values obtained from the previous iteration. The iterations proceed until the following criterion for the L_∞ norm is satisfied:

$$L_\infty = \frac{\max |\bar{h}^{n,m+1} - \bar{h}^{n,m}|}{\max |\bar{h}^{n,m+1}|} < 10^{-7} \quad (5)$$

for a fixed current time (n). The function \bar{h}^{n+1} for the new time will be acquired from $\bar{h}^{n,m+1}$, as soon as the criterion of convergence is satisfied.

2.3. The Splitting Scheme

The splitting of Eq. 3 is made according to the *second Douglas scheme* [16, 17]. Such strategy has been chosen to deal with the costly procedure of solving Eq. 3; even though we are working with sparse matrices for the operators, the internal iterations cause the process to be repeated several times during each time step. This problem welcomes an attempt to minimize the operations per unit iteration, as follows:

$$\frac{\tilde{h} - \bar{h}^n}{\Delta\tau} = \Lambda_X \tilde{h} + \Lambda_Y \bar{h}^n + f^{n+1/2} + (\Lambda_X + \Lambda_Y) \bar{h}^n \quad (6)$$

$$\frac{\bar{h}^{n,m+1} - \tilde{h}}{\Delta\tau} = \Lambda_Y (\bar{h}^{n,m+1} - \bar{h}^n). \quad (7)$$

Here, \tilde{h} is the height function for the intermediary time step. Equation 6 can be solved line by line and Eq. 7 can be solved column by column, which is one positive contribution of the splitting for the storage and precision of the resolution. In order to show that the splitting represents the original scheme, we rewrite Eqs. 6 and 7 in the form:

$$(E - \Delta\tau \Lambda_X) \tilde{h} = (E + \Delta\tau \Lambda_X) \bar{h}^n + 2\Delta\tau \Lambda_Y \bar{h}^n + \Delta\tau f^{n+1/2} \quad (8)$$

$$(E - \Delta\tau \Lambda_Y) \bar{h}^{n,m+1} = \tilde{h} - \Delta\tau \Lambda_Y \bar{h}^n \quad (9)$$

where E is the identity operator. The intermediate variable \tilde{h} is eliminated by applying the operator $(E - \Delta\tau \Lambda_X)$ to Eq. 9, and adding the result to Eq. 8:

$$(E - \Delta\tau \Lambda_X) (E - \Delta\tau \Lambda_Y) \bar{h}^{n,m+1} = (E + \Delta\tau \Lambda_X) \bar{h}^n + 2\Delta\tau \Lambda_Y \bar{h}^n + \Delta\tau f^{n+1/2} - (E - \Delta\tau \Lambda_X) \Delta\tau \Lambda_Y \bar{h}^n.$$

This result may be rewritten as:

$$\begin{aligned} [E - \Delta\tau (\Lambda_X + \Lambda_Y) + \Delta\tau^2 \Lambda_X \Lambda_Y] \bar{h}^{n,m+1} &= \\ [E + \Delta\tau (\Lambda_X + \Lambda_Y) + \Delta\tau^2 \Lambda_X \Lambda_Y] \bar{h}^n + \Delta\tau f^{n+1/2} & \end{aligned}$$

or either:

$$\begin{aligned} (E + \Delta\tau^2 \Lambda_X \Lambda_Y) \frac{\bar{h}^{n,m+1} - \bar{h}^n}{\Delta\tau} &= \\ (\Lambda_X + \Lambda_Y) (\bar{h}^{n,m+1} + \bar{h}^n) + f^{n+1/2}. & \end{aligned} \quad (10)$$

A comparison with Eq. 3 shows that Eq. 10 is actually equivalent to the original one, as their temporal
 130 order of approximation coincides. Note that the positive definite operator

$$B \equiv E + \Delta\tau^2 \Lambda_X \Lambda_Y = E + \mathcal{O}(\Delta\tau^2)$$

has a norm greater than one, acting on the discrete time derivative. This means that the operator B does not change the steady state solution. Furthermore, since $\|B\| > 1$, the scheme given by Eqs. 6-7 is more stable than the target one (Eq. 3).

2.4. The Method of Manufactured Solutions

The MMS is a code verification procedure, which analyzes if a numerical scheme and its implementation code stand for the task of representing the mathematical model of a physical event with sufficient accuracy.
 135 The idea behind the MMS is to solve a problem as if the analytical solution was available from start, creating a manufactured solution for a system of partial differential equations [18]. Considering that the proposed function is unlikely to solve the equations exactly, a residual term will appear due to the solution
 140 of the system. The insertion of such residue in the right-hand side of the equation as a source term leads to a different numerical solution, which is expected to approach the artificial analytical solution (if the manufactured equation was properly constructed).

Since the manufactured solution is defined on the continuum, the global discretization error can be examined by the discrete L_2 norm [19]:

$$L_2 = \left(\frac{\sum_{i=1}^N |\bar{h}_{i,k}^n - \bar{h}_{i,e}^n|^2}{N} \right)^{1/2} \quad (11)$$

145 where N is the total number of mesh nodes, i is the index of each node, and the indexes k and e represent the numerical and the manufactured (“exact”) solution, respectively. Such norm analyzes how the numerical solution approaches its corresponding analytical solution after each time step. It is indeed expected that the error will decrease by refining the mesh.

3. Linear Stability Analysis

150 Linear stability analysis is employed to study the system’s behavior when submitted to small perturbations, revealing whether the initial equilibrium point is stable or not. If an exponential growth is observed, such point is linearly unstable; on the other hand, if a exponential decay towards a steady state is found, that point is classified as linearly stable. For small perturbations, we may eliminate the non-linear terms from the governing equation, making the analytical analysis more straightforward. Equation 2 will take the form:
 155

$$\begin{aligned} \frac{\partial \bar{h}}{\partial \tau} = & -\alpha \bar{h} + \mu \frac{\partial^2 \bar{h}}{\partial X^2} + \bar{\nu} \frac{\partial^2 \bar{h}}{\partial Y^2} - D_{XX} \frac{\partial^4 \bar{h}}{\partial X^4} + D_{XY} \frac{\partial^4 \bar{h}}{\partial X^2 \partial Y^2} \\ & + D_{YY} \frac{\partial^4 \bar{h}}{\partial Y^4} - \bar{K} \left(\frac{\partial^4 \bar{h}}{\partial X^4} + 2 \frac{\partial^4 \bar{h}}{\partial X^2 \partial Y^2} + \frac{\partial^4 \bar{h}}{\partial Y^4} \right). \end{aligned} \quad (12)$$

Define a standard basis $\{\vec{1}_x, \vec{1}_y\}$ for the present Cartesian coordinate system. Considering $\bar{K} > 1$, a value of θ for $|\mu| > |\nu|$ (where $\nu = -c^2$), and a perturbation from the equilibrium state \bar{h}_o , we may write Eq. 12 in Fourier series:

$$\bar{h}(X, Y, t) = \sum_k \bar{h}_k e^{i(q_x X + q_y Y)} e^{\sigma_\tau t}$$

$$\sigma_\tau = [-\alpha + (-\mu q_x^2) + (-\nu q_y^2) - D_{XX}q_x^4 + D_{XY}q_x^2q_y^2 + D_{YY}q_y^4 - \bar{K}(q_x^2 + q_y^2)^2]$$

where \vec{q} are the spatial modes ($|q| = \sqrt{q_x^2 + q_y^2}$), and σ_τ is the growth rate (eigenvalue). The decomposition in Fourier modes is reasonable because the basis of trigonometric functions is appropriate to periodic structures. Since ν is negative for any θ , and μ is negative for $0 < \theta < 70.1^\circ$, we continue with the absolute values $|\mu|$ and $|\nu|$. The anisotropic coefficients D_{XX} , D_{XY} and D_{YY} can be hidden for an easier manipulation of the equation, observing that \bar{K} multiplies the same derivatives, as follows:

$$\sigma_\tau = -\alpha + |\mu|q_x^2 + |\nu|q_y^2 - \bar{K}(q_x^2 + q_y^2)^2. \quad (13)$$

This is an equation for the rate of growth of the mode \vec{q} . Consider $q^2 = q_x^2 + q_y^2$ for Eq. 13. Also, if we define the critical wavenumber as $q_c^2 = |\mu|/2\bar{K}$, the following expression is obtained:

$$\begin{aligned} \sigma_\tau &= (-\alpha + |\mu|q^2 - \bar{K}q^4) - (|\mu| - |\nu|) q_y^2 \\ &= \epsilon - \bar{K}(q^2 - q_c^2)^2 - (|\mu| - |\nu|) q_y^2 \end{aligned}$$

where $\epsilon = \mu^2/4\bar{K} - \alpha$. On decreasing α below $\mu^2/4\bar{K}$, a positive ϵ value is obtained. From this moment on, spatial modes with $\vec{q} = \pm q_c \vec{1}_x$ become unstable, while distancing from such values we remain in the stable domain. That is:

$$\sigma_\tau = \epsilon - \bar{K}(q_x^2 - q_c^2)^2 \implies q_x \approx q_c \text{ (for a small positive } \epsilon).$$

Reducing α even further, the unstable domain for $\vec{1}_x$ modes expands. For $\alpha = \nu^2/4\bar{K}$ and changing modes orientation up to $\vec{1}_y$, we can find that modes with $\vec{q} = \pm \sqrt{\nu/2\bar{K}} \vec{1}_y$ become first unstable in this direction. The calculation is performed as follows:

$$\begin{aligned} \sigma_\tau &= \frac{\mu^2 - \nu^2}{4\bar{K}} - \bar{K}(q^2 - q_c^2)^2 - (|\mu| - |\nu|) q_y^2 \\ &= \frac{\mu^2}{4\bar{K}} - \frac{\nu^2}{4\bar{K}} - \bar{k}q_y^4 + q_y^2|\nu| - \frac{\mu^2}{4\bar{K}} + q_y^2|\mu| - q_y^2|\nu| \\ &= -\frac{\nu^2}{4\bar{K}} - q_y^2(\bar{K}q_y^2 - |\nu|) \implies q_y = \pm \sqrt{\frac{\nu}{2\bar{K}}}. \end{aligned}$$

From the previous analysis, we can conclude that for $\alpha < \nu^2/4\bar{K}$, modes for all orientations will become unstable. However, it must be noticed that the maximum growth rate is limited to $q_c \vec{1}_x$, since the term $\bar{K}(q^2 - q_c^2)^2$ acts as a wave filter.

The linear stability analysis does not take into account weakly nonlinear effects. A more robust analysis of the prevailing structure should consider the interactions between different modes and the nonlinearities of the system. This coupling can be studied through amplitude equations. For the hexagonal structures, the modes are of equal amplitude, although presenting different wavevectors in order to deal with the anisotropy [20].

¹⁸⁰ **4. Weakly nonlinear Analysis**

Based on the linear stability analysis, for α in range $\nu^2/4\bar{K} \leq \alpha \leq \mu^2/4\bar{K}$ the maximum growth rate is associated with a $\vec{q} = q_c \vec{1}_x$ monomode pattern. Nevertheless, when we take into account nonlinear effects, this pattern may become unstable versus structures built on modes directly coupled through quadratic nonlinearities [21, 22]. The hexagonal modes are such that:

$$q_c \vec{1}_x + \vec{q}_2 + \vec{q}_3 = 0$$

¹⁸⁵ where q_c defines the critical circle $q_c = |\vec{q}_i|$, and \vec{q}_2 and \vec{q}_3 are defined as:

$$\begin{aligned} \vec{q}_2 &= q_{2x} \vec{1}_x + q_{2y} \vec{1}_y \\ \vec{q}_3 &= q_{3x} \vec{1}_x + q_{3y} \vec{1}_y . \end{aligned}$$

Therefore, $q_{2x} = q_{3x} = -q_c/2$ and $q_{2y} = -q_{3y} = \sqrt{3}q_c/2$. For critical hexagons, we propose the solution:

$$\bar{h} = \sum_n (A_n e^{i n \vec{q}_1 \cdot \vec{r}} + B_n e^{i n \vec{q}_2 \cdot \vec{r}} + C_n e^{i n \vec{q}_3 \cdot \vec{r}} + c.c.) .$$

Before moving to the amplitude equations, it is more straightforward to start analyzing from a critical ripple. The unidimensional evolution equation is given by:

$$\begin{aligned} \frac{\partial \bar{h}}{\partial \tau} &= -\alpha h + \mu \frac{\partial^2 h}{\partial X^2} + \bar{\nu}_x \left(\frac{\partial h}{\partial X} \right)^2 - \bar{K} \frac{\partial^4 h}{\partial X^4} \\ &= \epsilon h - \bar{K} \left(q_c^2 + \frac{\partial^2}{\partial X^2} \right)^2 h + \bar{\nu}_x \left(\frac{\partial h}{\partial X} \right)^2 \end{aligned}$$

¹⁹⁰ where $\epsilon = \mu^2/4\bar{K} - \alpha$, and $q_c^2 = |\mu|/2\bar{K}$ (the coefficient μ is negative for the angles of incidence covered in this work). Then, if we consider a solution of the form $h = A_1 e^{i q_c x} + A_2 e^{i 2q_c x} + \dots + c.c.$, the following results are obtained:

$$\begin{aligned} a) \quad \left(\frac{\partial \bar{h}}{\partial X} \right)^2 &= (i q_c A_1 e^{i q_c x} + i 2 q_c A_2 e^{i 2q_c x} + \dots + c.c.)^2 \\ &= (-q_c^2 A_1^2 e^{i 2q_c x} + 4 q_c^2 A_2 A_1^* e^{i q_c x} + \dots + c.c.) \end{aligned}$$

$$b) \quad \left(q_c^2 + \frac{\partial^2}{\partial X^2} \right)^2 A_2 e^{i 2q_c x} = (q_c^2 - 4 q_c^2)^2 A_2 e^{i 2q_c x} = -9 q_c^4 A_2 e^{i 2q_c x} .$$

Hence, the amplitude equations for A_1 and A_2 become:

$$\frac{\partial A_1}{\partial \tau} = \epsilon A_1 + 4 q_c^2 \bar{\nu}_x A_2 A_1^* + \dots \quad (14)$$

$$\frac{\partial A_2}{\partial \tau} = (\epsilon - 9 \bar{K} q_c^4) A_2 - q_c^2 \bar{\nu}_x A_1^2 + \dots \quad (15)$$

For slow variations of the amplitude, the time derivative in Eq. 15 becomes small when compared to the first two terms in the right-hand side such that we may write:

$$A_2 \approx \frac{q_c^2 \bar{\nu}_x A_1^2}{\epsilon - 9 \bar{K} q_c^4}.$$

¹⁹⁵ Hence, the amplitude A_2 adiabatically follows the amplitude A_1 as:

$$\frac{\partial A_1}{\partial \tau} = \epsilon A_1 - u |A_1|^2 A_1 + \dots, \quad \text{with } u \approx \frac{4 \bar{\nu}_x^2}{9 \bar{K}} \text{ for small } \epsilon.$$

Now, we move back to the critical hexagons. The evolution of A_1 behaves similarly to the critical ripples, and the only difference in the equation comes from the interaction between the second and the third modes. Note that the following terms are obtained:

$$a) \left(\frac{\partial \bar{h}}{\partial X} \right)^2 = -q_c^2 A_1^2 e^{i 2 q_c x} + 4 q_c^2 A_2 A_1^* e^{i q_c x} - \frac{1}{2} q_c^2 B_1^* C_1^* \epsilon^{i q_c x} + \dots + c.c.$$

$$b) \left(\frac{\partial \bar{h}}{\partial Y} \right)^2 = \frac{3}{2} q_c^2 B_1^* C_1^* \epsilon^{i q_c x} + \dots + c.c.$$

²⁰⁰ Since the same adiabatic elimination from the critical ripples applies from the critical ripples applies for $\partial A_2 / \partial \tau$, the amplitude equation for A_1 becomes:

$$\frac{\partial A_1}{\partial \tau} = \epsilon A_1 + \nu_A B_1^* C_1^* - u_A |A_1|^2 A_1 + \dots$$

where:

$$\nu_A = \frac{q_c^2}{2} (3 \bar{\nu}_y - \bar{\nu}_x), \quad \text{and } u_A \approx \frac{4 \bar{\nu}_x^2}{9 \bar{K}}. \quad (16)$$

Then, the amplitude equation for B_1 is obtained through the same procedure. The equations for the first two harmonics of this second mode are :

$$\begin{aligned} \frac{\partial B_1}{\partial \tau} &= (\epsilon - \Omega) B_1 + \nu_B A_1^* C_1^* + q_c^2 (\bar{\nu}_x + 3 \bar{\nu}_y) B_1^* B_2 + \dots \\ \frac{\partial B_2}{\partial \tau} &= (\epsilon - 4 \Omega - 9 \bar{K} q_c^4) B_2 - \frac{q_c^2 \bar{\nu}_x + 3 q_c^2 \bar{\nu}_y}{4} B_1^2 + \dots \end{aligned}$$

²⁰⁵ with $\Omega = \frac{3}{4}(|\mu| - |\nu|)q_c^2$ and $\nu_B = q_c^2 \bar{\nu}_x$. Once again, adiabatic elimination allows us to obtain the following relation between amplitudes:

$$B_2 \approx \frac{q_c^2 (\bar{\nu}_x + 3 \bar{\nu}_y)}{4(\epsilon - 4 \Omega - 9 \bar{K} q_c^4)} B_1^2.$$

Hence, the amplitude equation for B_1 is:

$$\frac{\partial B_1}{\partial \tau} = (\epsilon - \Omega)B_1 + \nu_B A_1^* C_1^* - u_B |B_1|^2 B_1 + \dots \quad (17)$$

$$\text{with } u_B \approx \frac{q_c^4(\bar{\nu}_x + 3\bar{\nu}_y)^2}{4(9\bar{K}q_c^4 + 4\Omega)} \text{ for small } \epsilon .$$

Similarly, the amplitude equation for C_1 is:

$$\frac{\partial C_1}{\partial \tau} = (\epsilon - \Omega)C_1 + \nu_C B_1^* A_1^* - u_C |C_1|^2 C_1 + \dots \quad (18)$$

where $\nu_C = \nu_B$ and $u_C = u_B$. Therefore, the resulting hexagonal patterns present a structure of the type:

$$h = A \cos(q_c x) + 2B \cos\left(\frac{1}{2} q_c x\right) \cos\left(\frac{\sqrt{3}}{2} q_c y\right).$$

In case the damping α is too low, Eqs. 16-17-18 do not hold to describe the resulting behavior, since an increasing number of harmonics may become unstable and more couples between smaller and larger scales will occur. However, if the damping is sufficiently high, the hexagonal structures should stabilize according to this weakly nonlinear analysis. For the numerical results that will be presented in the following sections, we were able to observe such hexagonal patterns for late time, based on the previously described triad of modes \vec{q}_1 , \vec{q}_2 , and \vec{q}_3 .

215 5. Code Verification

In consonance with the guidelines for the manufactured solution construction by Roache [23], an artificial solution was developed considering spatio-temporal variations of a surface:

$$\bar{h}_m = h_o + h_{xy} \sin\left(\frac{a_x \pi x}{L}\right) \cos\left(\frac{a_y \pi y}{L}\right) e^{bt}. \quad (19)$$

The parameter values employed in the manufactured solution and in the differential equation are presented on Table 1. Although the artificial solution does not need to be realistic for code verification, the chosen values were coherent with the studied simulations. Besides, the manufactured solution presents a periodic nature, which is also the case of the posed problem. All tests were run in a square domain with $L = 256$, and a time step of $\Delta\tau = 0.1$.

Table 1: Parameter values for the MMS

MS Parameters	Value	KS Parameters	Value
h_o	0	\bar{K}	5
h_{xy}	10^{-4}	a_η	4
a_x	2	θ	30°
a_y	2	α	0.15
b	-1/200		

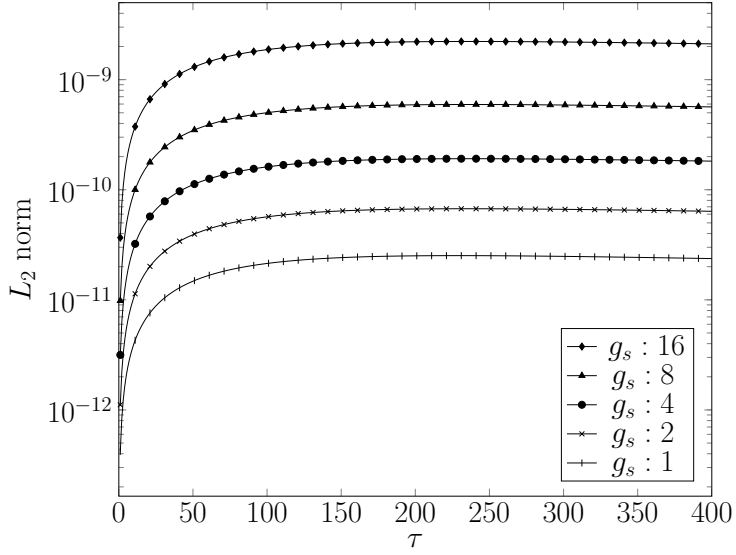


Figure 1: Evolution in time of the L_2 norm comparing different grid spacing g_s .

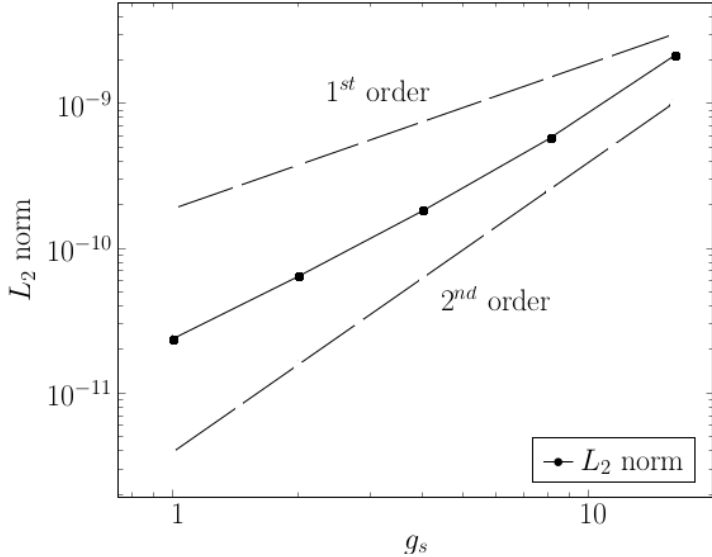


Figure 2: L_2 norm of the surface height for the manufactured solution. First and second order error lines are also displayed for comparison.

Figures 1 and 2 display how the spatial grid-refinement affects the global discretization error. The error tends toward second-order convergence with respect to grid spacing g_s for coarser meshes. However, as the grid gets more refined (smaller g_s), the error stands between first and second-order convergence.
225

The manufactured solution was unstable for the analyzed differential equation, which grows rapidly in time until its saturation, shadowing the contribution of the source term. For this reason, we limited the range of analysis to a stable region for the artificial function, where the numerical solution converges to the analytical solution. As we will later discuss, this region corresponds to a stage before the emergence of hexagonal modes.
230

6. Scheme Stability

One important issue which concerns the simulations is the time and mesh size selection, such that we seek reasonable choices inside the stable region of the present semi-implicit scheme. Here, we study the time step and grid spacing variation effect regarding the pattern evolution by tracking the L_1 norm evolution in time. During the simulations, we monitored the pattern's evolution by the L_1 norm rate of change in time, which indicates how fast the structure is changing between the current and previous time step, normalized by the spatial average of the surface height absolute value. This norm rate of variation is denoted as:

$$L_{1,t} = \frac{1}{\Delta\tau} \frac{\sum_{ij} |\bar{h}_{ij}^{n+1} - \bar{h}_{ij}^n|}{\sum_{ij} |\bar{h}_{ij}^{n+1}|}. \quad (20)$$

The computational effort was also measured, being related to the number of internal iterations when comparing results for a same grid spacing. Two different grids were used for the stability tests, as follows:

- 1. Case A: $\Delta X = \Delta Y = 2$, 64×64 points in a domain 128×128
- 2. Case B: $\Delta X = \Delta Y = 1$, 128×128 points in a domain 128×128

Both cases start with a monomodal initial pattern $q_0 \vec{1}_x$, presenting four wavelengths in the domain. The critical wavelength (related to the critical wavenumber q_c) is approximately 18: each of them would be represented by 9 points for Case A and by 18 points for Case B. The parameters adopted for the tests are displayed on Tab. 2.

Table 2: Parameters value and description

Parameter	Value	Description
α	0.15	damping coefficient
\bar{K}	5	surface diffusion effects
θ	30°	beam's angle of incidence
a_η	4	penetration depth/width of energy distribution

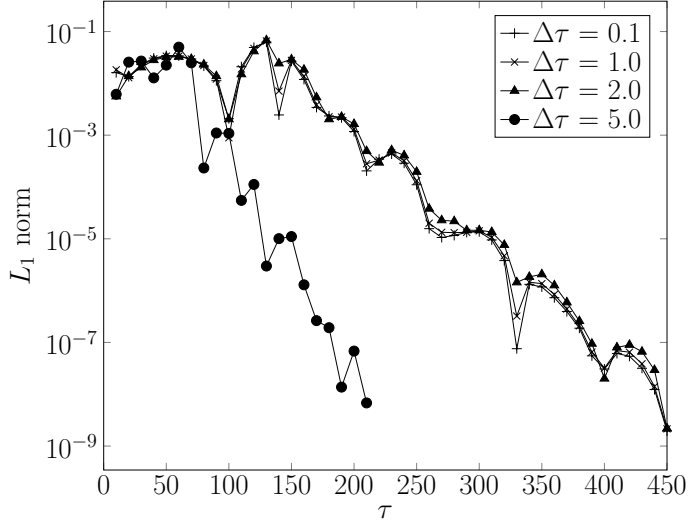
We assumed a pattern as stationary if the criterion $L_1 < 10^{-7}$ was reached for the temporal evolution. On the other hand, the simulation would be stopped if the L_1 curve demonstrated clearly a behavior converging to a fixed value (or oscillating around it). Even though $L_{1,t}$ is a rate of change and not the L_1 norm, we will refer $L_{1,t}$ just as L_1 for the sake of simplicity.

Figure 3 compares the structure evolution through the L_1 norm to observe when the results would diverge for an increasing time step.

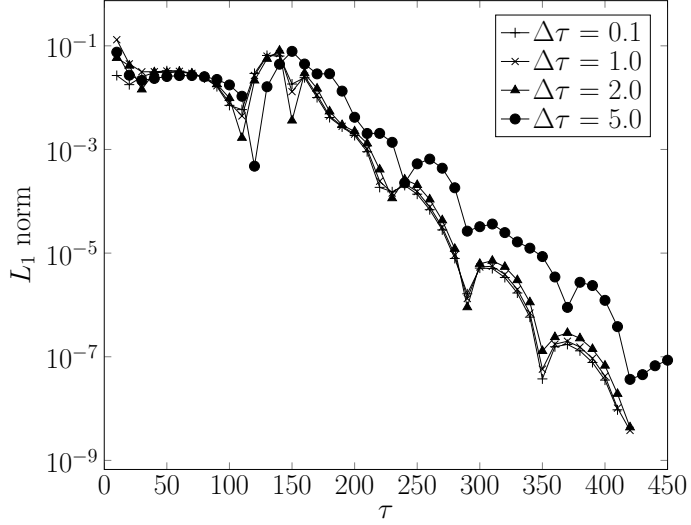
From Fig. 3a (Case A) we observe slight deviations in the L_1 norm evolution for $\Delta\tau = 2.0$ when comparing to inferior time steps values, while $\Delta\tau = 5.0$ diverges completely from the others. Regarding Fig. 3b (Case B), the divergence for $\Delta\tau = 5.0$ is also clear, but it's more coherent with the smaller time steps than Case A, as expected from a more refined mesh. This time, $\Delta\tau = 2.0$ is more consistent with the smaller ones, and would be accepted for the simulations. Even so, we decided to operate with up to $\Delta\tau = 1.0$ for both $\Delta X = 1$ and 2 , which is a more conservative approach. Nevertheless, represents a significant increase in time step (inside the stable domain) when compared to some of the aforementioned works that adopted explicit schemes [24, 14].

7. Anisotropic DKS evolution on preexisting patterns

Results regarding the evolution of the anisotropic DKS on preexisting patterns will be discussed next. The simulation results were obtained with the parameters \bar{K} , θ , a_η and α as shown in Tab. 2, using a mesh



(a) Case A: $\Delta X = 2$, 64×64 nodes in a domain 128×128



(b) Case B: $\Delta X = 1$, 128×128 nodes in a domain 128×128

Figure 3: L_1 norm as a measure for stability regarding time step.

consisting of 256×256 points, and a dimensionless grid spacing of $\Delta X = 2$. The reason for this choice is that K is given by:

$$K = \frac{D_s \rho n_d}{N^2 k_B T} \exp\left(-\frac{\Delta E}{k_B T}\right)$$

where D_s is the surface self-diffusivity, ρ is the surface free energy per unit area, n_d the density of diffusing atoms, N the atomic density, k_B the Boltzmann constant, ΔE the activation energy and T the temperature. We are particularly interested in high temperatures ($\bar{K} > 1$), such that diffusion is enhanced, acting on similar scales with sputtering terms. Then, by setting $T = 500$ K, we choose a realistic activation energy of $\Delta E = 1.25$ eV (typically in the range of 1 - 2.6 eV for small clusters of atoms), and do the same for the remaining parameters. This leads to the dimensionless $\bar{K} = 5$, and to the choice of $a_\eta = 4$. Specific

experimental systems can be studied by adjusting each of these parameters, depending for instance on the target material, and on the flux and energy of incoming ions. Those looking for further experimental data to perform simulations should visit some of aforementioned references [6, 13, 4].

7.1. [Case 1] Initial pattern with $\vec{q} = q_0 \vec{1}_X$, 2 wavelengths

We adopt an initial pattern consisting of an 1D structure with a wavenumber $q_0 = 2.4544 \cdot 10^{-2}$ in the $\vec{1}_X$ direction (2 starting wavelengths in the system), situated inside the stable domain. Figure 4 presents the time evolution of the L_1 norm, internal iterations, and maximum height $|\bar{h}^n|$ for this case, with a zoom into the initial regimes to display how the structure diminishes and rises.

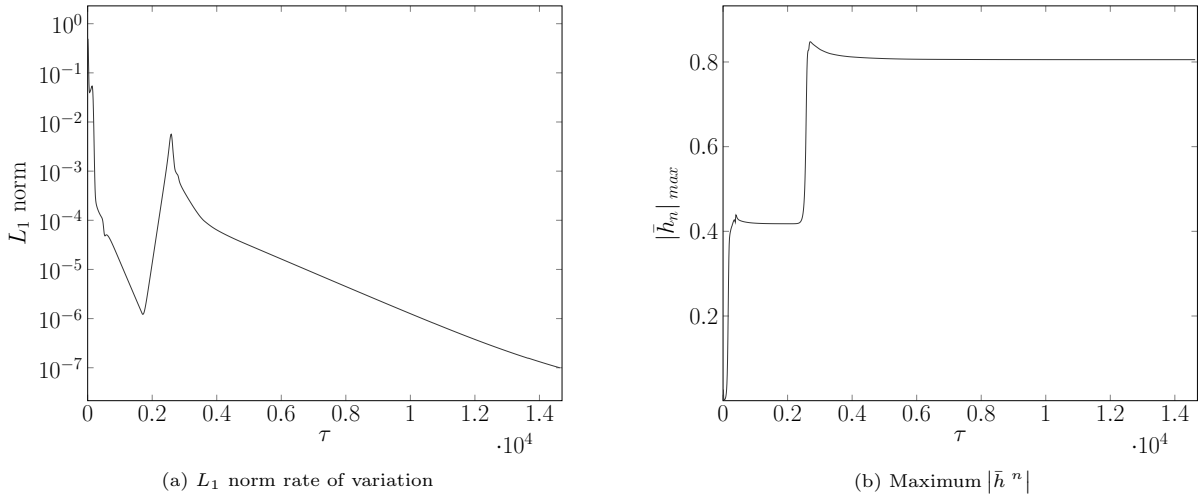


Figure 4: L_1 norm rate of variation, and maximum values for \bar{h}^n as a function of time τ , for an initial pattern with $\vec{q} = q_0 \vec{1}_X$ (inside the stable domain), $\Delta\tau = 0.1$, $\Delta X = \Delta Y = 2$, on a 256×256 nodes mesh. Beam angle is set at 30° .

From $\tau = 0$ to $\tau = 400$, it is possible to follow the nanostructuration of an 1D pattern with a wavenumber near q_c (upper panels of Fig. 5). Based on the L_1 curve and on the maximum absolute height value, one could think that a steady state was already reached about $\tau = 2,000$, since \bar{h}^n stabilized in a minimum of -0.42, and the pattern calmed down (see the continuous and pronounced fall of L_1). Nonetheless, after $\tau = 2,000$, the hexagonal modes emerge, and the 1D structure destabilizes. The L_1 curve rapidly ascends to its peak and then falls down, as the structure reorganizes and stabilizes with the new hexagonal pattern. A defectless nanohole pattern is attained for the steady state, with a minimum height frozen at -0.8, as seen in the lower panels of Fig. 5. The system is very sensitive to the initial wavenumber, and slight variations of q_c may lead to hexagonal patterns with remaining defects.

re

7.2. [Case 2] Initial pattern with $\vec{q} = q_0 \vec{1}_Y$, 2 wavelengths

The initial pattern for the second case is a monomodal $\vec{1}_Y$ surface, possessing the same number of wavelengths as Case 1, for the sake of comparison ($q_0 = 2.4544 \cdot 10^{-2}$). This wavenumber also lies in the linearly stable domain, so we expect a similar behavior of the dynamics during the first stage. Figure 6 contains the time evolution of the L_1 norm, internal iterations, and maximum height $|\bar{h}^n|$ for the second simulation. If we zoomed in the initial regimes, it would be possible to see the 1D structure diminishing in height before the emergence of hexagonal modes.

Case 2 does not display the formation of a 1D pattern with $\vec{q} \approx q_c \vec{1}_X$, as in Case 1. Between $\tau = 150$ and 200, the monomodal $\vec{1}_Y$ direction surface disappears, and new ripples start to proliferate in the domain. Figure 7 shows that these ripples quickly lose their orientation towards $\vec{1}_X$, and about $\tau = 750$ we already have the formation of nanoholes. Therefore, the nanohole structure takes over the system without an intermediate transition.

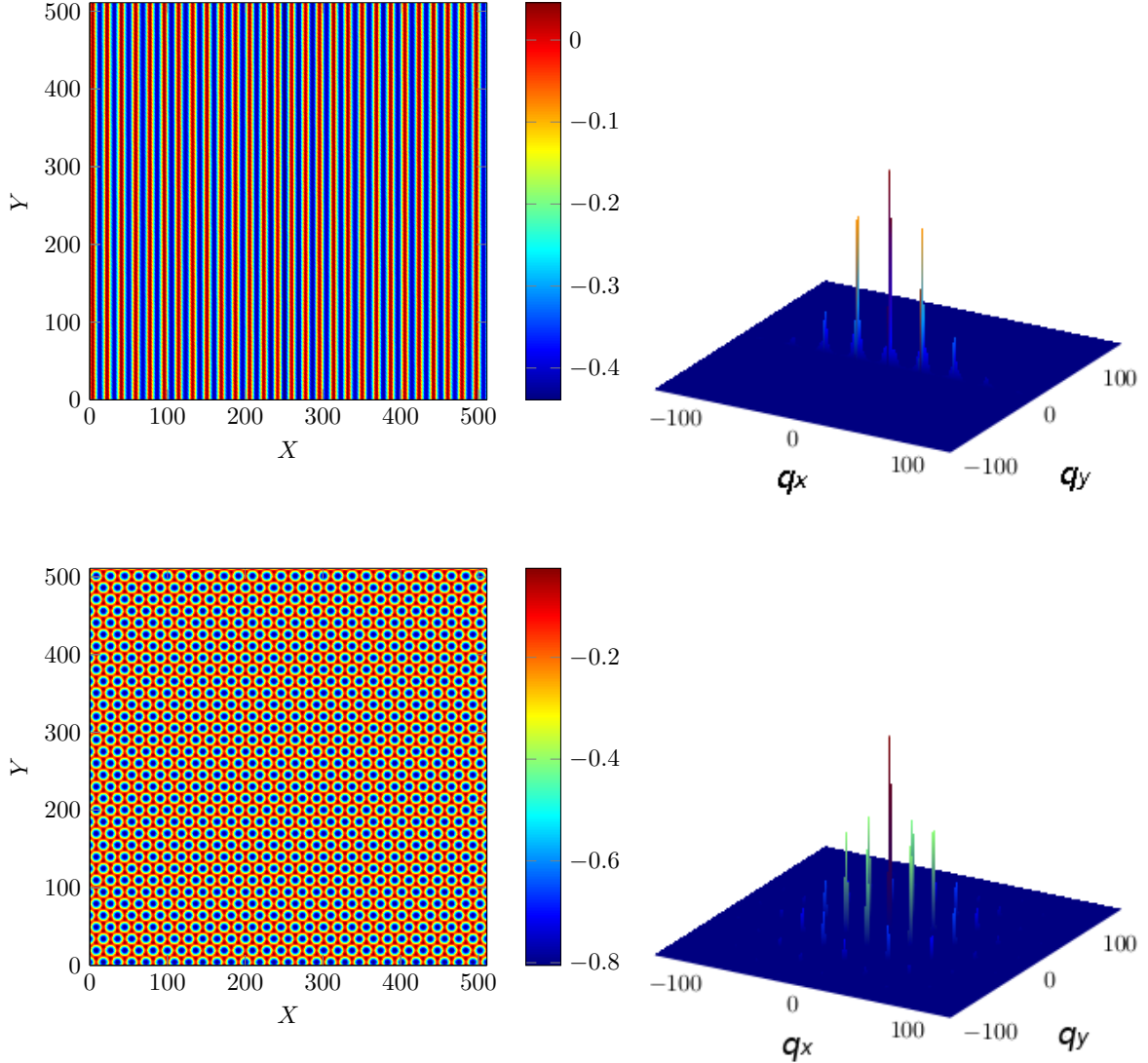


Figure 5: Surface height values \bar{h}^n and their respective Fourier Transform for $\tau = 400$ (upper panels) and $\tau = 14,630$, with an initial monomodal pattern presenting $\vec{q} = q_c \vec{1}_X$ and the beam angle set at 30° . The 1D structure is destabilized due to the emergence of the hexagonal modes.

The steady state (lower panels of Fig. 7) consists of a well ordered defectless nanohole pattern. Similarly to Case 1, this result is also physically consistent with the sputtering phenomenon, as the height decay is expected from the removal of surface atoms, alongside the rearrangement of the surface morphology. Besides, nanohole formation is one of the organized patterns achieved by ion beam sputtering.

305 7.3. Damping tests

The linear damping term had an essential contribution to the acquisition of the nanohole pattern, as seen in the last section. According to the previous work of Paniconi and Elder [24], three distinct solutions in the late time limit might be expected for the DKS equation, depending on the parameter α : periodic large hexagonal morphology for higher values, an oscillatory or breathing hexagonal state for middle values,

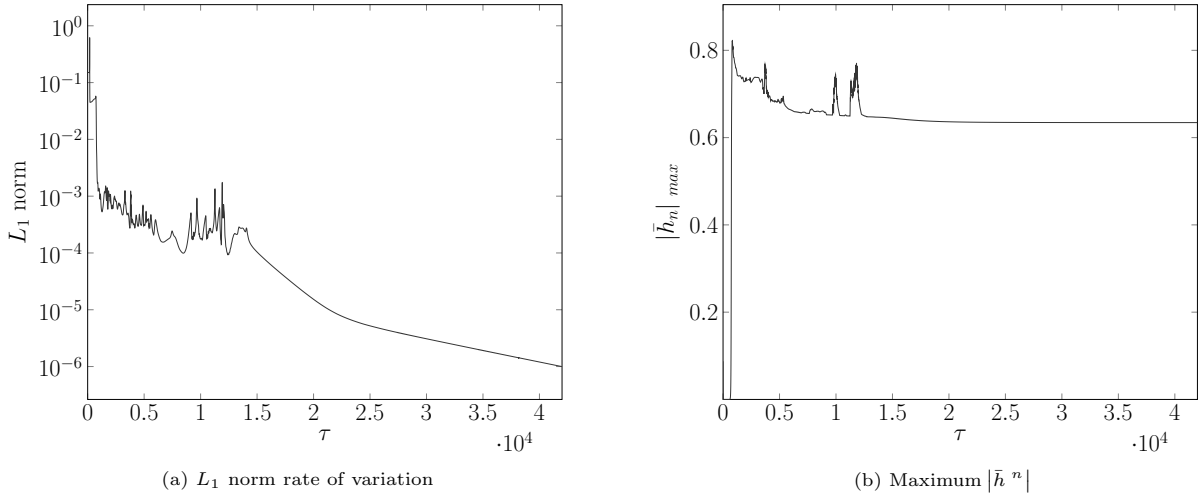


Figure 6: L_1 norm rate of variation, and maximum values for \bar{h}^n as a function of time τ , for an initial pattern with $\vec{q} = q_0 \vec{1}_Y$ (inside the stable domain), $\Delta\tau = 0.1$, $\Delta X = \Delta Y = 2$, on a 256×256 nodes mesh. Beam angle is set at 30° .

and a spatiotemporal chaotic state for lower values. However, since the present endeavor considers realistic coefficients related to the physics of sputtering, the range of α values employed by Paniconi and Elder would not produce the same effects. Besides, opposed to Paniconi and Elder, our study deals with an anisotropic DKS equation. Thereafter, during the first moments, linear effects lead to the selection of a well defined ripple direction; then, once nonlinear effects take over the system, cellular structures will develop (clearly seen on the results for $\alpha = 0.15$).

The undamped solution is shown in Fig. 8, for $\alpha = 0$. The initial condition presented a wavenumber $q_c = 1.7181 \cdot 10^{-1}$ (14 wavelengths in the system). A disordered chaotic cellular structure is obtained for late time, with large variations of cell size and shape, as displayed in Fig. 8a for $\tau = 11,803$. From the L_1 curve (Fig. 8b), we can see that the chaotic pattern is reached within $\tau = 500$. While a steady state isn't reached for the analyzed period, it's clear that the evolution dynamics are much slower during late time.

Figure 9 reveals the numerical solution for $\alpha = 0.05$. The initial condition was the same as the previous case ($q_c = 1.7181 \cdot 10^{-1}$). A spatiotemporal chaotic cellular structure is obtained for late time, which can be seen in Fig. 8a for $\tau = 11,750$. In comparison with the undamped structure, the late time pattern for $\alpha = 0.05$ is much more organized, with a smaller variation of cell sizes and shape, where some of them approach the critical λ_c width. The L_1 norm evolution (Fig. 9b) shows that a strongly oscillatory state is reached about $\tau = 2,000$, where L_1 starts fluctuating around $L_1 = 0.02$. These intense dynamics differ from the undamped case: even though the structure is more organized, it keeps changing at a constant rate for an undefined period of time.

Both cases differ from the simulation with $\alpha = 0.15$, where the damping effect is sufficient for an ordered and quick reorganization of the structure after a L_1 peak. In the $\alpha = 0.05$ case, the damping is not high enough to allow the microstructure to reorganize itself into a perfectly ordered hexagonal state, and it keeps chaotically oscillating around the peak L_1 value. Another observation is made towards the obtained height values: analyzing $\alpha = 0$ case, the mean height of the surface falls continuously with time, while maintaining the distance \bar{h}_{dif} between the minimum and maximum points around $\bar{h}_{dif} = 6.4$. However, for $\alpha = 0.05$, the mean height remains approximately constant, oscillating from -0.5 to -3.5 ($\bar{h}_{dif} \approx 3.0$), for an undefined time. In comparison, for the steady state obtained with a damping $\alpha = 0.15$ and $\vec{q} = q_0 \vec{1}_X$, the maximum and minimum height values were, respectively, -0.03 and -0.81 ($\bar{h}_{dif} = 0.78$).

The practical significance of those results is that the acquired structures might depend on the duration of the irradiation. For a short time duration sputtering in a system with $\alpha = 0.15$, we may have only ripple formation, while hexagons shall emerge for a longer duration of the experiment. In contrast, for a system with $\alpha = 0$ or 0.05, the final structure will depend on time, since it keeps changing with the irradiation

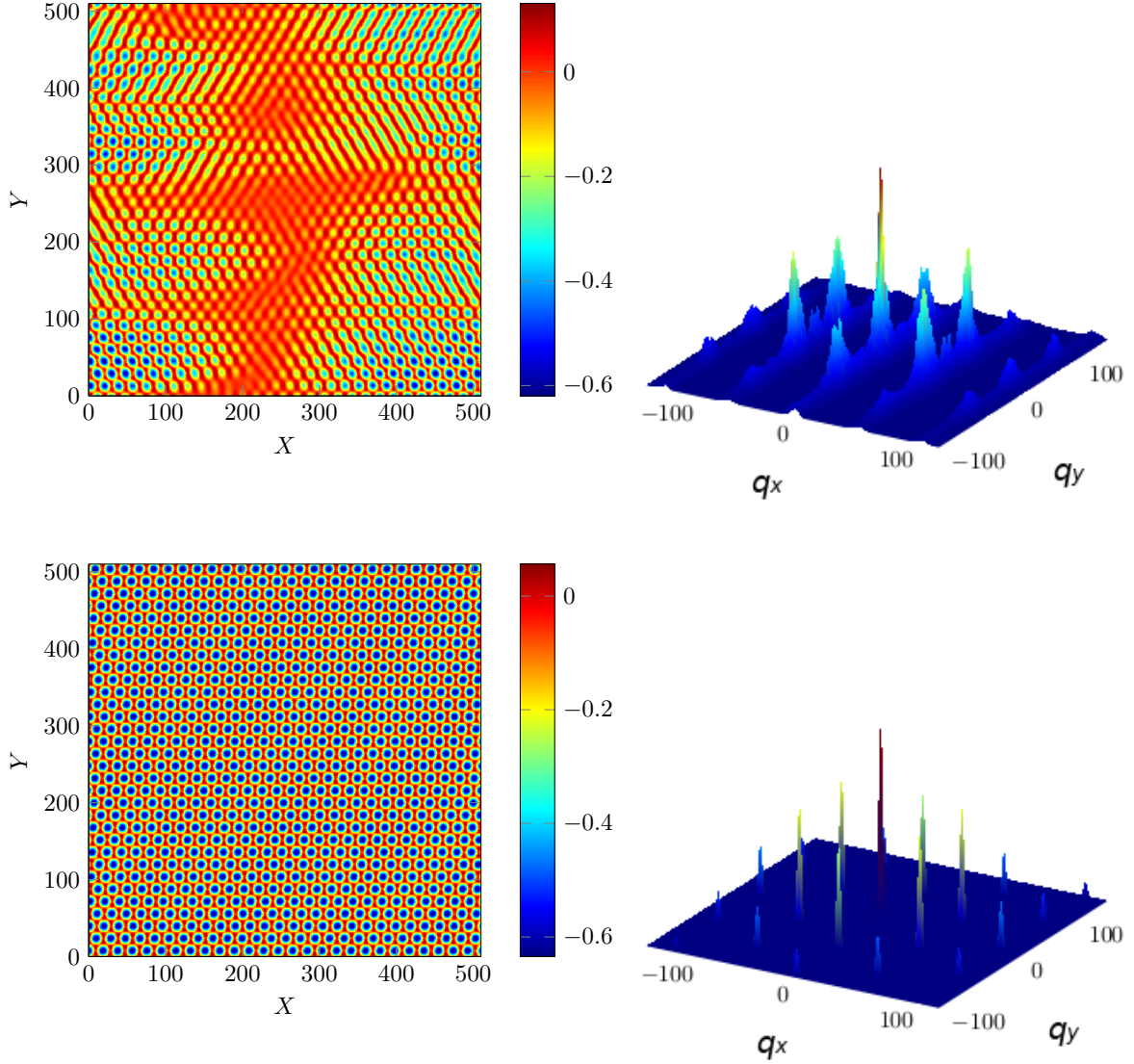


Figure 7: Surface height values \bar{h}^n and their respective Fourier Transform for $\tau = 750$ (upper panels) and $\tau = 40,000$, with an initial monomodal pattern presenting $\vec{q} = q_c \vec{1}_Y$ and the beam angle set at 30° . After the structure diminishes (while in the stable domain), the nonlinearities lead to the emergence of hexagonal modes, quickly dominating the entire system.

duration. We note that due to an unstable initial growth, the case without damping does not present proper physical results, since the magnitude of h grew surpassing reasonable boundaries. The curve L_1 for $\alpha = 0$ seems to decay in the long time, and further investigations could be made. Still, the present results reinforce the importance of the linear damping in the modelling of sputtering.

345

7.4. Anisotropy and angle of incidence

From our previous weakly nonlinear analysis, we are able to investigate the parameters involved in the relative anisotropy of the resulting patterns. The relative anisotropy is studied by $A = \Omega/\bar{K}q_c^4$, where q_c is the critical wavenumber obtained from our previous linear stability analysis, and $\Omega = \frac{3}{4}(|\mu| - |\nu|)q_c^2$. Figure 350 10 plots the relative anisotropy A versus θ for $\bar{K} = 5$ and $a_\eta = 4$. From the plot we observe that A for

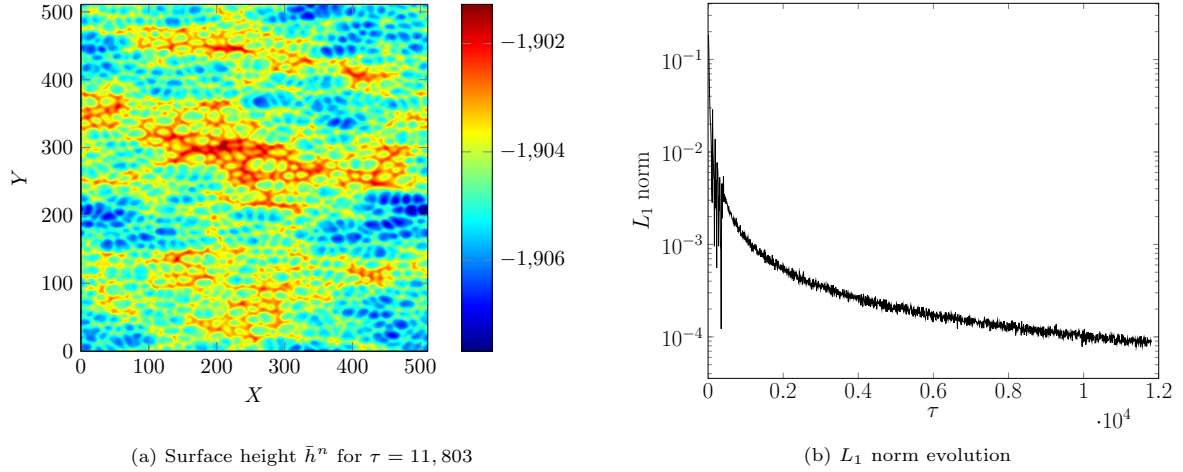


Figure 8: Numerical solution for a 2D anisotropic DKS equation - Spatiotemporal chaotic pattern, with $\alpha = 0$ and $\theta = 30^\circ$.

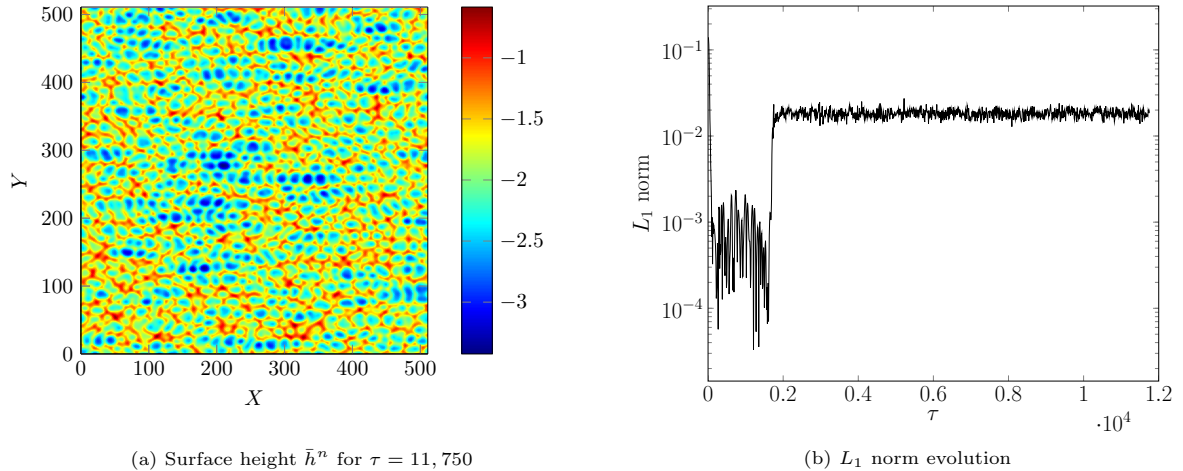


Figure 9: Numerical solution for a 2D anisotropic DKS equation - Chaotic semi-organized oscillatory behavior, with $\alpha = 0.05$ and $\theta = 30^\circ$.

$\theta = 0.5236$ (30°) is approximately 1.15, which was the value used up to this moment. The following results investigate the effect of varying the angle of incidence in the resulting pattern, motivated by this behavior of the relative anisotropy.

One region that we are particularly interested in is near $\theta = 1.2$, since $\bar{\nu}_x$ and $\bar{\nu}_y$ may present opposite signs with similar absolute value. This observation implies that there will be one direction for the unstable modes where the nonlinear terms ($\bar{\nu}_x$ and $\bar{\nu}_y$ from Eq. 2) will compensate each other, as studied in the work of Rost and Krug [7] (without damping). For such simulation, we set θ to 1.1549 (66.17°), which means that we will have the following anisotropy coefficients: $\bar{\nu}_x = 0.0658$ and $\bar{\nu}_y = -0.0659$. The damping coefficient is set to $\alpha = 0.1$.

Figure 11 shows that the nonlinearities compensate each other when the system remains aligned with the $\vec{1}_x$ direction, even for unstable modes. The nanostructure obtained for $\tau = 180$ is still irregular in terms of the ripple behavior, but the direction of preference is clear. There are approximately 23 wavelengths in the domain, which is less than the critical number of wavelengths from the linear stability analysis. In this case,

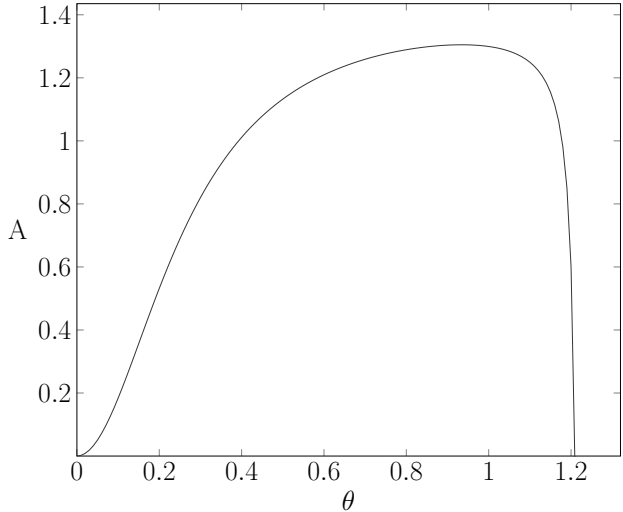


Figure 10: Relative anisotropy A versus θ for $\bar{K} = 5$ and $a_\eta = 4$.

we did not obtain a stationary structure, since the irregular ripple morphology keeps evolving, although the pattern's preferred direction remains the same.

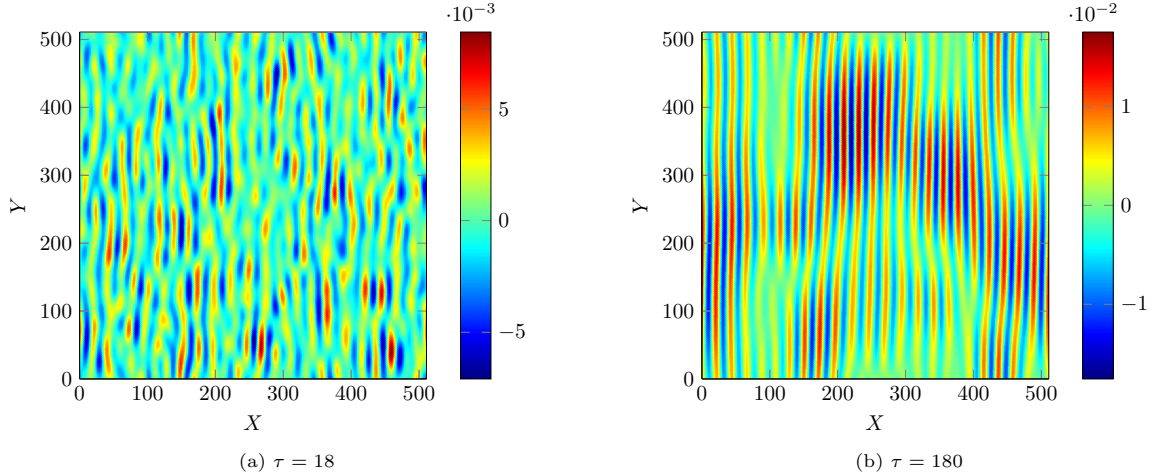


Figure 11: Simulation results for a system 512×512 with an angle $\theta = 66.17^\circ$. The nonlinearities “cancel” each other and a well defined direction arises from the unstable mode. This is made clear by the selection of the $\vec{1}_x$ direction for $\tau = 180$.

8. Conclusions

In the present work we have developed a finite-difference time splitting scheme to solve an anisotropic damped Kuramoto-Sivashinsky equation, which comes from the continuum theory and is an option to describe a surface eroded by ion bombardment. We dealt with realistic coefficients, based on physical values typically found in the literature. The dimensionless analysis was performed for a high temperature scenario ($T = 500K$).

The MMS was employed for code verification, and a second-order convergence was detected for coarser meshes comparison, while results between first and second-order convergence came up for more refined

375 meshes, suggesting a possible issue with the manufactured solution stability. Regarding the scheme's stability, the tests revealed that for $\Delta\tau \leq 2.0$, the numerical scheme was sufficiently stable with a grid spacing $\Delta X = 1.0$.

380 Spatiotemporal chaotic structures appeared for the undamped case, whose dynamics fell continuously for the long time. A chaotic oscillatory pattern rose from the simulation with $\alpha = 0.05$, reaching a better ordered structure than the one for the undamped result, while maintaining a pattern under oscillatory evolution after the emergence of the hexagonal modes. Defectless hexagonal periodic structures were obtained for higher values of the damping coefficient, with an angle of incidence $\theta = 30^\circ$. Although its physical origin has been questioned in the literature [25], the damping term is an essential ingredient of the present model to obtain the desired nanohole pattern.

385 Regarding the effect of preexisting patterns over the steady state in a system with higher damping coefficient ($\alpha \geq 0.1$), no appreciable difference was observed in the final morphology born from random or monomodal initial patterns. For all considered initial structures, we have arrived in the aforementioned defectless nanohole pattern. However, the evolution of \vec{I}_X monomodal patterns was significantly different when compared to the others, since the former was the only scenario where the nanostructuration of a 1D pattern with a wavenumber near q_c was observed before the emergence of hexagonal modes.

390 Based on the previous work of Rost and Krug, we investigated a case where the nonlinearities compensate each other. In their model, there was a subtle balance between the anisotropy of both the linear terms and nonlinear terms, leading to nonintuitive results, suggesting that a numerical analysis is essential. In this paper, the nonlinear compensation was achieved using $\theta = 66.17^\circ$, and an irregular oscillatory ripple structure with a clear orientation in the \vec{I}_X direction was obtained.

395 In summary, the studied model equation leads to ripple morphologies and nanohole patterns, such that the prevailing structure is sensitive to the anisotropy of the system, while unaffected by changes in the initial pattern. The hexagonal structures are equally attained through experiments, and the present results reinforce the role of the irradiation duration for the acquired surface morphology.

Acknowledgement

400 Eduardo Vitral acknowledges a fellowship from the Coordination for the Improvement of Higher Education-CAPES (Brazil). A FAPERJ Senior Researcher Fellowship is acknowledged by José Pontes. Gustavo Anjos is granted by Science Without Borders/Young Talent Attraction program (CAPES).

References

References

- 405 [1] E. Chason, W. L. Chan, Spontaneous patterning of surfaces by low-energy ion beams, in: Materials Science with Ion Beams, Springer, 2010, pp. 53–71.
- [2] R. Gago, L. Vázquez, O. Plantévin, J. Sánchez-García, M. Varela, M. Ballesteros, J. Albella, T. Metzger, Temperature influence on the production of nanodot patterns by ion beam sputtering of Si (001), *Physical Review B* 73 (15) (2006) 155414.
- 410 [3] Q. Wei, X. Zhou, B. Joshi, Y. Chen, K.-D. Li, Q. Wei, K. Sun, L. Wang, Self-assembly of ordered semiconductor nanoholes by ion beam sputtering, *Advanced Materials* 21 (28) (2009) 2865–2869.
- [4] U. Valbusa, C. Boragno, F. B. de Mongeot, Nanostructuring surfaces by ion sputtering, *Journal of Physics: Condensed Matter* 14 (35) (2002) 8153.
- [5] S. A. Mollick, D. Ghose, B. Satpati, Formation of Au-Ge nanodots by Au- ion sputtering of Ge, *Vacuum* 99 (2014) 289–293.
- [6] M. A. Makeev, R. Cuerno, A.-L. Barabási, Morphology of ion-sputtered surfaces, *Nuclear Instruments and Methods in Physics Research Section B: Beam Interactions with Materials and Atoms* 197 (3) (2002) 185–227.
- [7] M. Rost, J. Krug, Anisotropic Kuramoto-Sivashinsky equation for surface growth and erosion, *Physical review letters* 75 (21) (1995) 3894.
- 415 [8] C. Christov, J. Pontes, D. Walgraef, M. G. Velarde, Implicit time splitting for fourth-order parabolic equations, *Computer methods in applied mechanics and engineering* 148 (3) (1997) 209–224.
- [9] C. Christov, J. Pontes, Numerical scheme for Swift-Hohenberg equation with strict implementation of Lyapunov functional, *Mathematical and computer modelling* 35 (1) (2002) 87–99.

- [10] P. Sigmund, Theory of Sputtering. i. Sputtering yield of amorphous and polycrystalline targets, *Physical Review* 184 (1969) 383–416.
- [11] R. M. Bradley, J. M. Harper, Theory of ripple topography induced by ion bombardment, *Journal of Vacuum Science & Technology A* 6 (4) (1988) 2390–2395.
- [12] R. Cuerno, A.-L. Barabási, Dynamic scaling of ion-sputtered surfaces, *Physical review letters* 74 (23) (1995) 4746.
- [13] A. Keller, S. Facsko, Ion-induced nanoscale ripple patterns on Si surfaces: theory and experiment, *Materials* 3 (10) (2010) 4811–4841.
- [14] S. Facsko, T. Bobek, A. Stahl, H. Kurz, T. Dekorsy, Dissipative continuum model for self-organized pattern formation during ion-beam erosion, *Physical Review B* 69 (15) (2004) 153412.
- [15] R. M. Bradley, Redeposition of sputtered material is a nonlinear effect, *Physical Review B* 83 (7) (2011) 075404.
- [16] J. Douglas, H. H. Rachford, On the numerical solution of heat conduction problems in two and three space variables, *Transactions of the American mathematical Society* (1956) 421–439.
- [17] N. N. Yanenko, *The method of fractional steps*, Springer, 1971.
- [18] N. Malaya, K. C. Estacio-Hiroms, R. H. Stogner, K. W. Schulz, P. T. Bauman, G. F. Carey, MASA: a library for verification using manufactured and analytical solutions, *Engineering with Computers* 29 (4) (2013) 487–496.
- [19] C. J. Roy, Review of code and solution verification procedures for computational simulation, *Journal of Computational Physics* 205 (1) (2005) 131–156.
- [20] N. Ghoniem, D. Walgraef, *Instabilities and Self-organization in Materials*, Oxford Univ. Press, 2008.
- [21] D. Walgraef, Nano-patterning of surfaces by ion sputtering: A proposal for a numerical study of the effect of preexisting patterns, working notes, unpublished.
- [22] P. Manneville, *Dissipative structures and weak turbulence*, San Diego, CA (USA); Academic Press Inc., 1990.
- [23] P. J. Roache, Code verification by the method of manufactured solutions, *Journal of Fluids Engineering* 124 (1) (2002) 4–10.
- [24] M. Paniconi, K. Elder, Stationary, dynamical, and chaotic states of the two-dimensional damped kuramoto-sivashinsky equation, *Physical Review E* 56 (3) (1997) 2713.
- [25] R. M. Bradley, P. D. Shipman, Spontaneous pattern formation induced by ion bombardment of binary compounds, *Physical review letters* 105 (14) (2010) 145501.